

Optical Engineering

OpticalEngineering.SPIEDigitalLibrary.org

Review of profiling oceanographic lidar

James H. Churnside

Review of profiling oceanographic lidar

James H. Churnside

NOAA Earth System Research Laboratory
325 Broadway
Boulder, Colorado 80305
E-mail: james.h.churnside@noaa.gov

Abstract. This paper provides a review of the development of profiling oceanographic lidars. These can provide quantitative profiles of the optical properties of the water column to depths of 20 to 30 m in productive coastal waters and to depths of 100 m for a blue lidar in the open ocean. The properties that can be measured include beam attenuation, diffuse attenuation, absorption, volume scattering at the scattering angle of 180 deg, and total backscattering. Lidar can be used to infer the relative vertical distributions of fish, plankton, bubbles, and other scattering particles. Using scattering as a tracer, lidar can provide information on the dynamics of the upper ocean, including mixed-layer depth, internal waves, and turbulence. Information in the polarization of the lidar return has been critical to the success of many of these investigations. Future progress in the field is likely through a better understanding of the variability of the lidar ratio and the application of high-spectral-resolution lidar to the ocean. Somewhat farther into the future, capabilities are likely to include lidar profiling of temperature in the ocean and an oceanographic lidar in space. © *The Authors*. Published by SPIE under a Creative Commons Attribution 3.0 Unported License. Distribution or reproduction of this work in whole or in part requires full attribution of the original publication, including its DOI. [DOI: [10.1117/1.OE.53.5.051405](https://doi.org/10.1117/1.OE.53.5.051405)]

Subject terms: oceanography; lidar; ocean optics; remote sensing; polarization; fisheries; plankton; internal waves.

Paper 131053SS received Jul. 12, 2013; revised manuscript received Nov. 4, 2013; accepted for publication Nov. 7, 2013; published online Dec. 6, 2013; corrected Jul. 11, 2017.

1 Introduction

There are very few options available to probe the interior of the ocean remotely. Both active and passive acoustics have been widely used, but are limited by the almost total reflection of acoustic energy from the air/water interface. As a result, acoustic systems must be in contact with the water. Electromagnetic systems are limited by the high absorption of sea water except for a narrow region in the blue-green portion of the visible spectrum, and both active and passive sensors have been developed to operate in this spectral region. Optical systems are useful not only as alternatives for airborne and satellite sensors, but also where acoustic systems could be deployed, since they respond to different constituents within the water.

The ability to measure ocean color globally from satellites has revolutionized scientific understanding of the biogeochemistry of the upper ocean on a global scale.^{1,2} This is largely through the inference of concentrations of chlorophyll-*a* contained within phytoplankton. These studies have described the global spatial distributions, seasonal cycles, and decadal trends in phytoplankton concentrations. Coupled with other information, ocean color estimates of chlorophyll concentration can be used to estimate the primary productivity,^{3,4} which is the rate of conversion of CO₂ into organic matter, of the ocean over the same spatial and temporal scales. However, ocean color measurements can provide only limited information about the depth distribution of ocean constituents.

Lidar has the capability to provide information about the depth distribution of optical scattering, and this review will concentrate on those applications of oceanographic lidar that produce depth-resolved profiles of various constituents of the ocean. This excludes some very successful applications that

include underwater target detection and identification,⁵⁻⁷ bathymetry,^{8,9} laser-induced fluorescence,¹⁰⁻¹² and surface-roughness measurements.¹³⁻¹⁵ Information about these applications can be found in the cited references.

2 Hardware Considerations

The most common type of lidar for oceanographic applications has used green polarized light. Such a lidar can be assembled from commercial components and can be made very robust for operation in harsh environments. It can easily be designed to operate from a small aircraft, since it would require <1 kW of power, would weigh <100 kg, and would have a volume <0.5 m³.

The essential components of the lidar transmitter are the laser and standard beam conditioning optics. The most common source is a Q-switched, frequency-doubled, Nd:YAG laser, operating at a wavelength of 532 nm. Pulse length is typically 1 to 10 ns, which corresponds to a range resolution of 0.11 to 1.1 m in seawater. When flashlamp-pumped, these lasers can produce 100 to 500 mJ pulses at repetition rates of 10 to 100 Hz. Diode-pumped lasers are also available; these are generally suitable when a higher repetition rate at lower pulse energy is desired.

The choice of the 532 nm wavelength is largely because of the availability of an efficient, compact, rugged laser at 532 nm. The absorption of light in pure seawater^{16,17} has its lowest value at a wavelength of 450 nm, which is 0.3 times the value at 532 nm. As the concentrations of other constituents like phytoplankton, colored dissolved organic material (CDOM), and detritus increase, the wavelength of minimum absorption shifts toward the green. The absorption of CDOM and detritus at 450 nm are 3 times¹⁸ and 2.5 times¹⁹ the corresponding values at 532 nm. A model for absorption that

uses chlorophyll concentration as a parameter for the absorption by all organic constituents¹⁶ suggests that the absorption will be less at 532 nm than at 450 nm whenever the chlorophyll concentration is $>1 \text{ mg m}^{-3}$. The average surface-chlorophyll concentration from all MODIS-AQUA data (Fig. 1) suggests that the 532 nm wavelength is quite good for much of the coastal ocean. Although a shorter wavelength will be better for open-ocean applications, the absorption at 532 nm is only 40% greater than that at 450 nm for a chlorophyll concentration of 0.3 mg m^{-1} , and use of 532 nm may not be a bad compromise for much of the global ocean.

One of the most critical parameters on the lidar receiver side is the dynamic range; the rapid attenuation of light in water implies a large dynamic range is necessary to achieve good depth penetration. For example, 80 dB of receiver dynamic range will allow penetration to $>46 \text{ m}$, where the attenuation coefficient is $<0.1 \text{ m}^{-1}$. This can be accomplished directly by a high-speed digitizer with 13.5 bits of effective dynamic range. It can also be accomplished using a digitizer with less dynamic range if the signal dynamic range can be compressed or split into a high-gain channel and a low-gain channel that are digitized separately and combined in processing. Dynamic-range compression can be accomplished with a logarithmic amplifier,²⁰ by increasing the photomultiplier tube gain with time to match the signal decay²¹ or by using a feedback circuit on the photomultiplier tube gain to obtain a logarithmic response.²² All of these approaches are made difficult by the high frequencies ($>250 \text{ MHz}$) required for most profiling applications. Multiple channels with different gains can be obtained by splitting the electronic signal from the photomultiplier anode^{23,24} or by taking one signal from the anode and one from a dynode where the total gain is lower.²⁵

The other parameter that must be given serious consideration is the field of view. The amount of background light collected by the receiver is low when a very narrow field of view and a very narrow-band interference filter are used. However, this configuration produces the most rapid attenuation of the lidar signal. A wider field of view will reduce the attenuation in water and may lessen laser safety concerns.

However, the amount of background light will be increased both because more background light is collected and because a wider interference filter bandwidth might be required to accommodate the larger incidence angles. The latter effect is because the filter response will shift to shorter wavelengths for non-normal incidence by an amount $\Delta\lambda = (1/2)\lambda_0\xi_i^2/n_e^2$, where λ_0 is the wavelength at normal incidence, ξ_i is the incidence angle at the filter, and n_e is the effective refractive index of the cavity (generally between 1.5 and 2).²⁶ A 1-nm filter will have an acceptance angle near 100 mrad, depending on n_e .

The level of background light will depend on conditions, but is generally limited by the reflection of the sky from the surface. The direct reflection of the Sun from the surface produces very high background signals and is generally avoided. In clear skies, the diffuse light at the surface will generally be $<1.5 \text{ Wm}^{-2} \text{ nm}^{-1}$,²⁷ producing an unpolarized reflected spectral radiance (at 532 nm) of $\sim 10 \text{ mWm}^{-2} \text{ sr}^{-1} \text{ nm}^{-1}$.

3 Lidar Signal

3.1 Basic Characteristics

If a lidar is directed into the water through the surface, the first interaction will be the Fresnel reflection from the air/water interface, which has a refractive index of ~ 1.33 . For normal incidence on a flat sea, the Fresnel reflection is 2%, which will create a very large surface return in the lidar receiver, but the loss of energy in the subsurface return caused by two-way transmission through the surface is only 4%. The reflection for unpolarized light is $<5\%$ until the incidence angle reaches $\sim 60^\circ$. Thus, surface losses can generally be neglected, although the surface return can be quite large.^{13,28,29}

Neglecting the effects of multiple scattering, the depth-dependent lidar signal can be described by the lidar equation.

$$S(z) = \frac{EAO(z)T_oT_s^2\eta v}{2n(nH+z)^2}\beta(\pi, z)\exp\left[-2\int_0^z\alpha(z')dz'\right] + S_B, \quad (1)$$

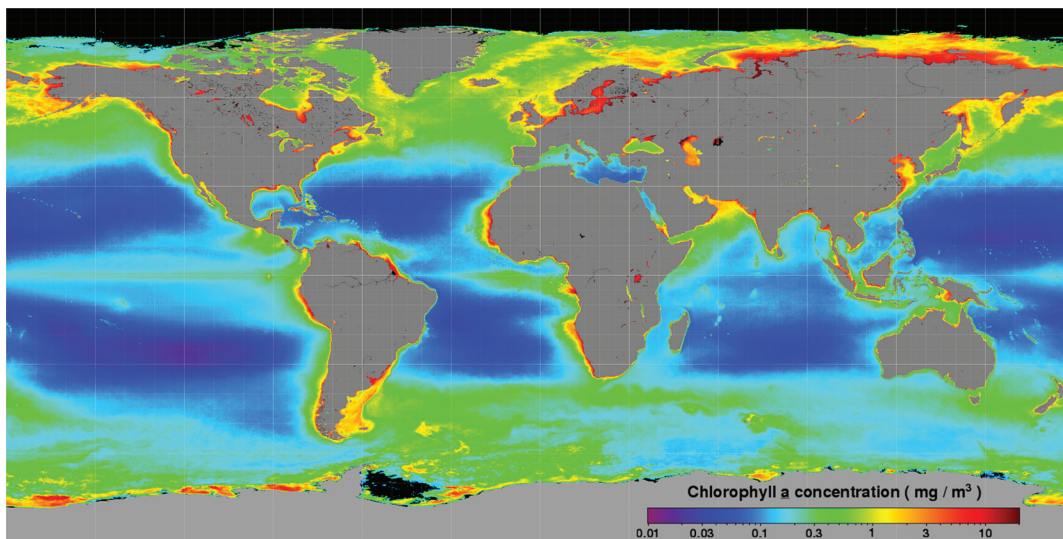


Fig. 1 Mission-averaged MODIS AQUA chlorophyll concentration as of April 30, 2013. Absorption at 532 nm is within 40% of that at 450 nm for chlorophyll concentration $>0.3 \text{ mg m}^{-3}$ (areas of green to red on the map). (Image courtesy of NASA, <http://oceancolor.gsfc.nasa.gov>).

where S is the detector photocathode current, E is the transmitted pulse energy, A is the receiver area, O is the lidar overlap function (also known as the geometric form function), T_O is the transmission of the receiver optics, T_S is the transmission through the sea surface, η is the responsivity of the photodetector (A W^{-1}), n is the refractive index of sea water, v is the speed of light in vacuum, H is the distance from the lidar to the surface (height of the aircraft for near-nadir airborne systems), z is the path length in water (depth for near-nadir airborne systems), β is the volume scattering coefficient at a scattering angle of π radians, α is the lidar attenuation coefficient, and S_B is the photocurrent due to background light.

The effects of multiple scattering on the lidar signal have been calculated using a number of approaches. One straightforward technique is Monte Carlo, in which a large number of individual photons are tracked through random paths based on the statistical properties of the medium.³⁰⁻³² Starting at the surface and continuing at each scattering event, random numbers determine the distance and direction to the next event. For the distance, l , a random number is selected from the probability-density function.

$$p(l) = b \exp(-bl), \quad (2)$$

where b is the scattering coefficient. The probability-density function for the scattering angle is

$$p(\theta, \phi) = \frac{\beta(\theta)}{b}, \quad (3)$$

where θ is the magnitude of the scattering angle and ϕ is the azimuth. The azimuthal angle is selected from a uniform distribution. For unpolarized light, β does not depend on ϕ . For polarized light, β depends on the plane of polarization relative to ϕ .^{33,34} In principle, the calculation continues until the photon passes through the plane of the receiver, where it is weighted by a factor $\exp(-\sum a_i l_i)$, where a_i is the absorption coefficient along the i 'th path segment (of length l_i). In practice, it is generally necessary to enhance the occurrence of low-probability backscattering events and compensate for this with an additional weighting factor.

Another approach is to find approximate solutions to the radiative-transfer equation for monochromatic light.³⁵

$$\begin{aligned} \frac{n}{v} \frac{\partial}{\partial t} L(r, s, t) + s \cdot \nabla L(r, s, t) \\ = -cL(r, s, t) + \oint \beta(s \rightarrow s') L(r, s', t) ds', \end{aligned} \quad (4)$$

where n is the refractive index of sea water, v is the speed of light in vacuum, L is radiance, r is the three-dimensional position vector, s is the three-dimensional direction vector, t is time, and the extinction coefficient, $c = a + b$. One such approach is the discrete-ordinates method,^{36,37} which has been applied to the lidar case using the Lobatto quadrature.³⁸ Another approach to radiative transfer is the successive order of scattering,^{39,40} in which single scattering, double scattering, triple scattering, etc., are treated independently and the results summed. Because of absorption in the ocean, the contribution from higher-order multiple scattering drops relatively quickly with the scattering order and only a

few terms are necessary, but it is not clear that this technique has been applied to oceanographic lidar.

Arguably, the most successful approach uses the quasi-single scattering approximation,⁴¹⁻⁴³ which takes into account the fact that most scattering in the ocean is at very small scattering angles. In many cases, Eq. (1) is still valid as long as the appropriate attenuation coefficient is used.⁴⁴ If the transmitter beam divergence and receiver field of view are very narrow, the appropriate attenuation coefficient is the beam attenuation coefficient c . If the transmitter beam divergence and receiver field of view are much greater than the forward peak of the scattering phase function, the appropriate attenuation coefficient will be the diffuse attenuation coefficient K_d , neglecting solar zenith angle effects on K_d . For airborne systems, the diffuse attenuation coefficient is also appropriate for narrow angles if the lidar spot diameter on the surface is much greater than the inverse of the beam attenuation coefficient. Monte-Carlo calculations showing this effect³¹ can be approximated by the following equation:

$$\alpha = K_d + (c - K_d) \exp(-0.85cD), \quad (5)$$

where D is the lidar spot diameter on the surface and the single-scattering albedo is approximated by $\omega_0 = 1.14(1 - K_d/c)$. The original calculations (reproduced in Fig. 2) were performed using two scattering phase functions, measured in the Sargasso Sea at 460 and 655 nm. While the results at the two wavelengths are slightly different, Eq. (5) is generally between them and is probably a reasonable approximation for 532 nm. This figure suggests that α will be near K_d for cD greater than two or three.

The diffuse attenuation coefficient can be estimated from the absorption coefficient and the backscattering coefficient, b_b , which is given by

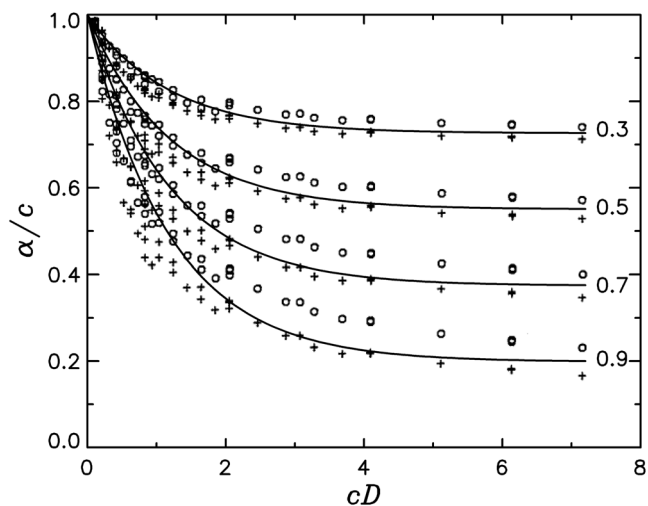


Fig. 2 Monte-Carlo calculations of lidar attenuation coefficient, α , normalized by beam attenuation coefficient, c , for specific phase functions measured at 460 nm (o) and 655 nm (+) (reproduced from Ref. 31). The labels refer to the value of single-scattering albedo, ω_0 , used for the calculations. Solid lines provide the approximation of Eq. (5).

$$b_b = 2\pi \int_{\pi/2}^{\pi} \beta d\theta. \quad (6)$$

It is tempting to argue that photons are lost when they are absorbed or scattered by angles such that $\theta > \pi/2$, so $K_d = a + b_b$. A more rigorous estimate yields $K_d = 1.04(a + b_b)$,⁴² which suggests that the simple argument is not too far off. An even more detailed comparison with model calculations produced a slightly more complicated formula.⁴⁵

$$K_d = a + 4.18b_b[1 + 0.52 \exp(-10.8a)]. \quad (7)$$

At the commonly used wavelength of 532 nm, $a > 0.052 \text{ m}^{-1}$, so $K_d - a$ is between $4.18b_b$ and $5.42b_b$. Equation (7) is consistent with recent measurements of lidar attenuation.²⁸

The background current S_B is given by

$$S_B = \pi\phi_R^2 A \Delta\lambda T_0 \eta L_B, \quad (8)$$

where ϕ_R is the half-angle field of view of the receiver, $\Delta\lambda$ is the bandwidth of the optical filter, and L_B is the spectral radiance of the background light. This background can easily be estimated for each lidar pulse,²³ since the first term in Eq. (1) becomes very small at large depths.

Equation (1) suggests a complex dependence of performance on lidar parameters and the characteristics of the water column. A complete investigation of lidar design trade-offs is beyond the scope of this paper, but the effects of field of view are particularly interesting. The example will use typical lidar parameters: $\lambda = 532 \text{ nm}$, $E = 100 \text{ mJ}$, $A = 79 \text{ cm}^2$ (10 cm diameter telescope), $O = 1$, $T_0 = 0.5$, $\eta = 43 \text{ mA W}^{-1}$ (10% quantum efficiency), $H = 300 \text{ m}$, and a noise bandwidth of 500 MHz. Two different water types will be considered using parameters from Ref. 17: coastal with $\beta(\pi) = 1 \times 10^{-3} \text{ m}^{-1} \text{ sr}^{-1}$, $K_d = 0.19 \text{ m}^{-1}$, $c = 0.40 \text{ m}^{-1}$ and open ocean with $\beta(\pi) = 5 \times 10^{-4} \text{ m}^{-1} \text{ sr}^{-1}$, $K_d = 0.057 \text{ m}^{-1}$, $c = 0.15 \text{ m}^{-1}$. Background light is taken to be $10 \text{ mW m}^{-2} \text{ sr}^{-1} \text{ nm}^{-1}$.²⁷ A narrow field-of-view receiver is assumed to have $\phi = 1 \text{ mrad}$ and $\Delta\lambda = 0.1 \text{ nm}$ so that $\alpha = c$. A wide field-of view receiver with $\Delta\lambda = 1 \text{ nm}$ is assumed to have $\phi = 10 \text{ mrad}$ for coastal applications and $\phi = 100 \text{ mrad}$ for open ocean applications so that $\alpha = K_d$ in both cases.

A rough estimate of depth penetration can be obtained by considering the depth at which the laser signal falls below the larger of the background-light signal and the shot noise of the combined signal. For the wide field of view, this depth is 27 m for the coastal example and 45 m for the open-ocean example; it is limited by the background light level. For the narrow field of view, the corresponding depths are 15 and 36 m and are limited by the noise level. Even these depths may be difficult to reach, however, since 100 dB of receiver dynamic range would be required to profile from the surface to 15 m in the coastal ocean and 94 dB to reach 36 m in the clear ocean with a narrow field of view. Dynamic range considerations for the wide field of view are much less stringent.

The conclusion is that a wide field-of-view lidar can reach greater depths than one with a narrow field of view. The quasi-single scattering approximation provides an efficient technique to model the performance of such a system. In

this approximation, the lidar attenuation can be approximated by K_d as long as cD is >2 to 3, and the resulting lidar can be expected to penetrate 20 to 30 m in coastal waters and 40 to 50 m in open-ocean waters.

3.2 Polarization Effects

Polarization has proven to be an important tool in oceanographic lidar. There are two phenomena that depolarize a lidar signal when the source laser is polarized. Many scattering particles in the ocean are not homogeneous spheres, but are sufficiently irregular that the backscattered light will be partially depolarized, even at a scattering angle of 180 deg. These include objects of practical interest like fish, zooplankton, and large phytoplankton. In addition, multiple forward scattering will partially depolarize light, even for ideal homogeneous spheres.

In the quasi-single-scattering approximation, the components of the received lidar signal copolarized with the transmitted laser and in the orthogonal polarization can be expressed as⁴⁶

$$\begin{aligned} S_C(z) &= \frac{EAO(z)T_0T_S^2\eta v}{2n(nH+z)^2} f_C(\pi, z)\beta(\pi, z) \exp\left[-2\int_0^z \alpha(z')dz'\right] \\ S_X(z) &= \frac{EAO(z)T_0T_S^2\eta v}{2n(nH+z)^2} \left[f_X(\pi, z)\beta(\pi, z) \right. \\ &\quad \left. + 2\int_0^z \gamma(z')dz' f_C\beta(\pi, z) \right] \exp\left[-2\int_0^z \alpha(z')dz'\right], \quad (9) \end{aligned}$$

where f_C is the fraction of light at depth z that is copolarized with the incident light after scattering by π radians, $f_X = 1 - f_C$ is the fraction that is scattered into the orthogonal polarization, and γ is the rate at which light is depolarized by multiple forward scattering. The depolarization ratio of the lidar return is then given by

$$\frac{S_X(z)}{S_C(z)} = \frac{f_X(\pi, z)}{f_C(\pi, z)} + 2\int_0^z \gamma(z')dz', \quad (10)$$

as long as all of the system parameters, including the overlap function, are the same for both receiver channels. Where the scattering properties of the water do not change with depth, Eq. (10) suggests that γ is half of the derivative of depolarization ratio with respect to z .

In principle, β , f_C , f_X , and γ can be calculated for linear or circular polarization if the concentrations and structures of all of the scattering particles are known. The quantities $f_C\beta$ and $f_X\beta$ can be obtained from single-scattering calculations of the polarization-dependent backscatter cross-sections and concentrations of each type of particle. In practice, these calculations are difficult for the complex, nonspherical particles found in the ocean. The simplifying assumption of homogeneous spherical particles cannot be used because it produces the result that $f_X = 0$, which is contrary to observations. The multiple-scattering depolarization parameter, γ , can be obtained from polarization-dependent radiative-transfer calculations. In this case, the assumption of spherical particles can be used to obtain an approximate solution, since this calculation will produce depolarization.

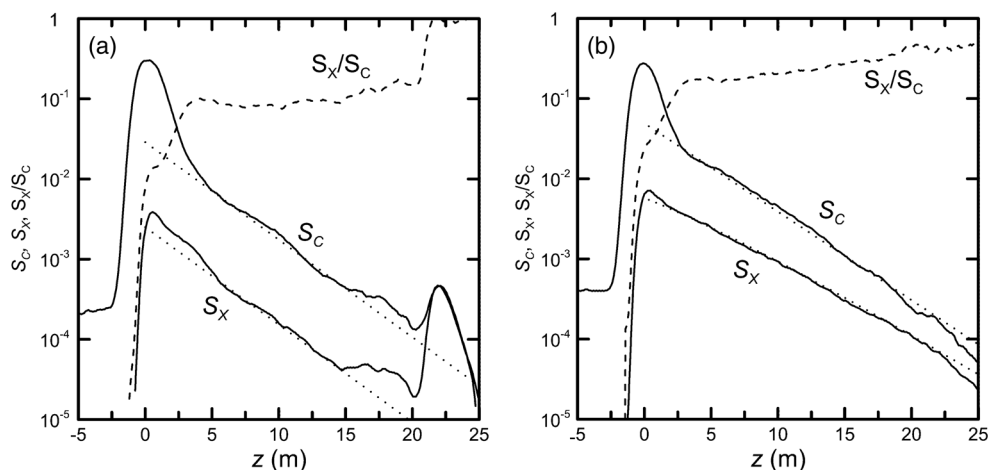


Fig. 3 Examples of copolarized lidar depth profile, S_C (upper solid line), simultaneous cross-polarized profile, S_X (lower solid line), corresponding predictions from Eq. (7) assuming uniform water characteristics (dotted lines), and measured depolarization ratio, S_X/S_C (dashed line) for (a) near shore and (b) offshore. (Reproduced from Ref. 46).

Examples of lidar depth profiles for linear polarizations are plotted in Fig. 3 for two different cases.⁴⁶ Both cases show the high surface return in the copolarized signal that is not included in Eq. (9). For the near-shore case, the attenuation of both channels is about the same (0.14 m^{-1}), and the depolarization rate, γ , is nearly 0. The depolarization is $\sim 10\%$ except for the highly polarized surface return and the highly depolarizing bottom return at a depth of 22 m. For the offshore case, the copolarized attenuation is only slightly less at 0.13 m^{-1} , but this includes more scattering and less absorption than the near-shore case (a higher single-scattering albedo). In this case, the attenuation of the cross-polarized signal is less because of a nonzero depolarization rate of $\gamma = 6.1 \times 10^{-3} \text{ m}^{-1}$.

The use of circular polarization can produce larger depolarization ratios, but no additional information. For backscattering (at 180°) from a collection of particles with mirror symmetry, van de Hulst used symmetry arguments to show that the Mueller matrix would be diagonal.⁴⁷ It was later shown that these diagonal elements were related as^{48,49}

$$\mathbf{M} = \beta(\pi) \begin{bmatrix} 1 & 0 & 0 & 0 \\ 0 & 1 - \delta & 0 & 0 \\ 0 & 0 & \delta - 1 & 0 \\ 0 & 0 & 0 & 2\delta - 1 \end{bmatrix}, \quad (11)$$

where $\beta(\pi)$ is the unpolarized volume backscatter coefficient at 180° and δ is the single polarization parameter, which has been described⁴⁹ as “a measure of the propensity of the scattering medium to depolarized the incident polarization.” This implies that the depolarization of an initially polarized beam will be

$$\frac{S_{XL}}{S_{CL}} = \frac{\delta}{2 - \delta}, \quad \frac{S_{XC}}{S_{CC}} = \frac{\delta}{1 - \delta}, \quad (12)$$

where the first letter in the subscript refers to the co- (C) or cross-polarized (X) signal and the second to linear (L) or circularization (C). Because there is only one parameter related to depolarization, however, the contrast between large scattering particles and the background scattering level is the

same whether linear or circular polarization is used;⁴⁹ this has been verified experimentally.⁵⁰

Thus, the quasi-single-scattering approximation can be applied to polarized lidar, with the general result that the information content is the same whether linear or circular polarization is used. However, Eq. (12) shows that the signal level in the cross-polarized channel will be greater when circular polarization is used, which implies a higher signal-to-noise ratio.

3.3 Laser Safety

Oceanographic lidars operate with intense pulses of visible light, and ocular safety must be considered. The single-pulse exposure limit is 5 mJ m^{-2} .⁵¹ For a typical pulse energy of 100 mJ, this implies that the laser spot diameter needs to be $>5 \text{ m}$ to be safe for direct viewing. To calculate the exposure for light reflected from the surface, the Fresnel reflection coefficient and the surface roughness should be included.⁵²

For exposure to multiple pulses, the exposure limit should be reduced by $N_p^{-0.25}$, where N_p is the number of pulses. For an airborne system, N_p is unlikely to be more than two or three as the illumination moves swiftly. For a lidar on a ship, N_p is generally taken as the number of pulses within the average response time of 0.25 s.

Where the exposure would be above the limit, access must be limited or protective eyewear used. Often, this can be accomplished by an observer who can stop laser transmission if someone is about to come into the danger zone. For low-level flights of the NOAA lidar, the system is designed to be eyesafe at the sea surface, and the pilot is provided with a remotely controlled laser shutter to use in the event of aircraft below the flight altitude.

Marine mammals in the study area present another set of issues. There are regulations for both ship and aircraft operations to prevent harassment of marine mammals. Marine mammals are less susceptible to ocular damage than humans,⁵³ so a system that is eyesafe at the surface according to the standards will not cause damage to marine mammals.

Note that this information is provided as a general overview and is not a substitute for a thorough analysis based on

published standards such as ANSI Z136.1 (Ref. 54) and Z136.6 (Ref. 55).

4 Applications

4.1 Fisheries

The advantages of airborne lidar for fisheries surveys are that large areas can be covered quickly (before the fish move) and at lower cost than with a surface vessel.²³ The feasibility of detecting fish schools with an airborne lidar was studied in 1974.⁵⁶ As early as 1976, an U.S. Navy airborne lidar was used to detect fish south of Florida.⁵⁷ The next year, the same system measured vertical profiles of fish schools off New Jersey.⁵⁷ A ship-based lidar was used to detect fish in cages in 1978.⁵⁸ This early work demonstrated that lidar could be useful for fisheries applications, and this has been confirmed by several subsequent analyses.^{32,59,60}

The easiest case is when large fish are widely separated, so individuals can be seen in the return and counted. As an example, Fig. 4 presents the depths and positions of 69 individual fish that were detected using the cross-polarized lidar signal at night off the Oregon coast.⁶¹ During the day, only two individual fish were detected along the identical flight track, suggesting a species that is at depth during the day and near the surface at night. No fish were detected within the cold water of the upwelling zone within 40 km of the coast. These characteristics suggest that most of these fish are likely albacore tuna (*Thunnus alalunga*). The density of fish detected beyond the upwelling zone during this survey was 25.6 ± 3.1 fish km^{-2} , where the uncertainty was estimated assuming a random distribution of fish within the survey area.

More work has been done on the harder problem of quantitative estimates of populations of schooling fish species, where many individuals are within the illuminated region for each shot. In this case, we note that β in Eq. (1) is the sum of a fish component, β_F , and a water component, β_W , which includes everything else. To estimate β_F , we have to filter the data in some way to separate the two components. Depending on conditions, we can assume that the water component does not vary with depth or that it has some

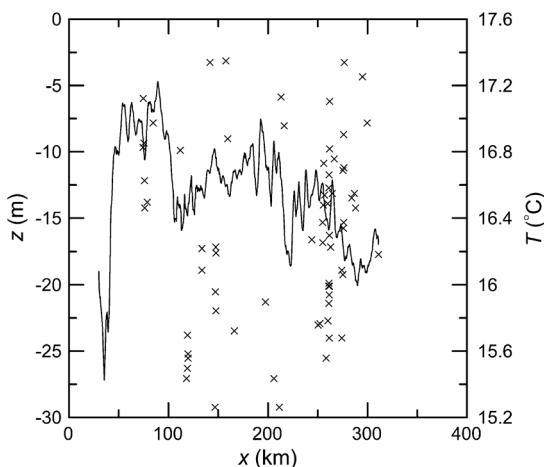


Fig. 4 Depth, z , and position, x (km from the coastline along 46°N latitude), of individual fish detected (symbols). Line is sea-surface temperature, T , measured by an infrared radiometer on the same aircraft.

depth profile that does not vary horizontally over some distance that is large compared with the horizontal extent of the fish schools.²³ In either case, we can apply a filter and a threshold to remove small signals to estimate β_F and α . To increase the contrast between the fish and water components, the cross-polarized component is generally used. The technique of applying a filter and threshold is then used to obtain $f_{XF}\beta_F$, where f_{XF} is the cross-polarized fraction of the return from fish. Figure 5 shows an example for a school of sardines (*Sardinops sagax*) observed by airborne lidar.⁶¹

There have been a number of validation tests to establish a correlation between lidar results and traditional acoustic and trawl techniques using a relative value of $f_{XF}\beta_F$ instead of an absolute value. The correlation approach is attractive because it does not require absolute calibration of the lidar or target strength estimates of the fish species involved. It does require estimation of, and correction for, attenuation. When individual schools were identified visually and targeted by both lidar and acoustics, the correlation was very high (0.994).⁶² Comparisons have also been made using data from the same area, but taken at different times. In these cases, correlations with acoustics^{24,63} and with trawls^{61,64} were both lower, but >0.5 as long as the time difference was less than four days and appropriate filtering and threshold values were applied.

A more difficult step is to convert an absolute value for $f_{XF}\beta_F$ into a biomass estimate. This requires calibration of the lidar to get the absolute value of $f_{XF}\beta_F$ and estimates of the target strength and average mass of the target species. The biomass density (kg m^{-3}) can be found from

$$M_F = \frac{m_F f_{XF} \beta_F}{\text{BRDF}_X A_F}, \quad (13)$$

where m_F is the mass of an individual fish, A_F is the cross-sectional area of a single fish, and BRDF_X is the cross-polarized fraction of the average bidirectional reflectance distribution function of a single fish for polarized lidar illumination, measured at the lidar observation angle. The product $\text{BRDF}_X A_F$ is target strength, which has been measured for several species of dead fish.^{65,66} More reliable measurements have been made using live sardines,²⁰ mackerel,⁶⁷ and menhaden.⁶⁸

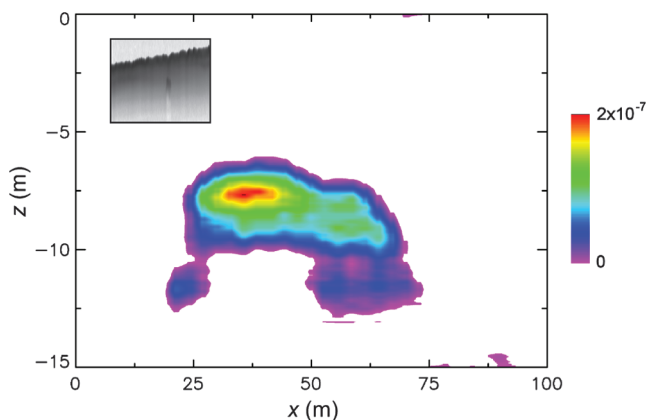


Fig. 5 Calibrated cross-polarized lidar return, $f_X \beta$ (values in $\text{m}^{-1} \text{sr}^{-1}$ according to the color bar on the right), from a school of sardines versus depth, z , and distance along the flight track, x . Inset is section of raw lidar data before correction for attenuation and calibration.⁶¹

Similar techniques have been used to detect large zooplankton, although the details of filtering and the thresholds used are different. With appropriate processing, a correlation of 0.78 was obtained between lidar and acoustic measurements of copepods in Prince William Sound, Alaska.⁶⁹

In addition to biomass estimates for fisheries management, lidar can be used to investigate aspects of fish behavior. For example, lidar data were used with those from an infrared radiometer on the same aircraft to show that sardines were associated with thermal fronts in the NE Pacific Ocean,⁷⁰ validating an earlier prediction.⁷¹ Lidar data were used with visual observations to show the evolution of a foraging event involving whales, seabirds, herring, and euphasiids in the SE Bering Sea.⁷² Evidence that fish near the surface avoid research vessels that are trying to measure their abundance has also been observed, in agreement with other methods.⁷³

4.2 Scattering Layers

Lidar is also able to profile optical scattering layers in the upper ocean, whether operating from a ship⁷⁴ or aircraft.⁷⁵ Most of these layers are phytoplankton and comprise large, nonspherical algal cells. Individual cells can be longer than 1 mm, and multicell colonies even larger. The structures can be very complex, which results in high-order multiple scattering within individual cells. As a result, these layers are more detectable in the cross-polarized return of a polarized lidar than in the copolarized return or in an unpolarized lidar.^{32,76,77}

Of particular importance are thin plankton layers,^{78–81} in which high concentrations of nutrients and phytoplankton are found in a thin layer often associated with the pycnocline. These layers can be as little as 10 cm thick, yet extend for km and persist for days. These concentrated layers can affect the biogeochemical processes in the upper ocean, including primary productivity and the formation of harmful algal blooms.

Airborne lidar data were used to investigate the occurrence of thin layers and mechanisms of formation,⁷⁷ with the result that layers were found to be associated with

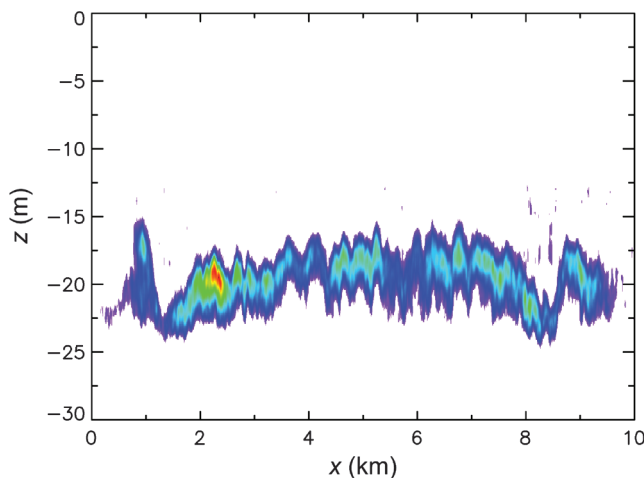


Fig. 6 Thin plankton layer within a warm-core eddy in the Gulf of Alaska versus depth, z , and distance along the flight track, x . Data are uncalibrated, but relative values follow the same color scale as Fig. 5. (Reproduced from Ref. 77).

wind-driven and topographic upwelling, fresh-water influx, and warm core eddies. Figure 6 shows an example of a plankton layer within a warm-core (anticyclonic) eddy in the Gulf of Alaska.⁷⁷ The mechanism for the productivity of warm-core eddies is an area of active investigation,^{82,83} and the discovery of thin layers on the scale shown in the figure may provide important information.

Plankton layers also affect retrievals based on passive optical measurements.^{84,85} Comparisons between lidar measurements, *in-situ* measurements, and the statistics of variability in passive measurements have been used to investigate some of these effects.^{86,87}

4.3 Optical Properties

Another application of lidar is the inference of the optical properties of sea water, at least at the laser wavelength. From Eq. (1), it is evident that two properties of the water contribute to the signal—the lidar attenuation and the volume backscattering coefficient, so the problem is ill posed and suitable inversion techniques must be applied. The most common technique in atmospheric lidar is to assume a value for the ratio $\alpha/\beta(\pi)$, known as the lidar ratio. This ratio will change with the type of scatterers, but is relatively unaffected by changes in number density or atmospheric absorption (negligible at common lidar wavelengths). For example, six aerosol types are defined for the cloud-aerosol lidar and infrared pathfinder satellite observations (CALIPSO) lidar, and a fixed lidar ratio is used for each.⁸⁸ The variety of scattering particles in the ocean is much larger, however, so measuring the lidar ratio for each type is not a practical approach.

Although sophisticated inversion techniques have been developed for atmospheric lidar, the same cannot be said for oceanographic lidar retrievals. Where the optical properties are not changing with depth, as in a surface mixed layer, the lidar signal will exhibit an exponential decrease with depth (e.g., Fig. 3). The lidar attenuation is easily estimated from the slope of that decrease, even for an uncalibrated system.^{46,89} Generally, the attenuation of the lidar signal is between the beam attenuation, c , and the diffuse attenuation, K_D , as expected from the discussion in Sec. 3.^{28,31,90,91} This suggests that either or both of the attenuation coefficients could be inferred with the appropriate lidar geometry.

It may also be possible to infer the absorption coefficient from the lidar attenuation coefficient by considering the relationship between volume backscatter and attenuation in a particular area. A linear relationship between attenuation and backscattering, as in Fig. 7, would suggest that the absorption coefficient can be estimated from the limiting lidar attenuation with no backscatter.⁴⁶ Intercept values are 0.27, 0.12, and 0.06 m^{-1} for the Columbia River plume, near-shore water outside of the plume, and offshore water, respectively. These values are about what would be expected for absorption coefficient at 532 nm, although direct comparisons of lidar and *in-situ* measurements are needed to confirm the relationship. This example was only done for the near-surface layer, but there is no reason that the technique cannot be extended to obtain profiles of absorption coefficient.

One reason for interest in the absorption coefficient is that it can provide a measure of the amount of dissolved organic material in milligrams of carbon per liter (mgC L^{-1}). The

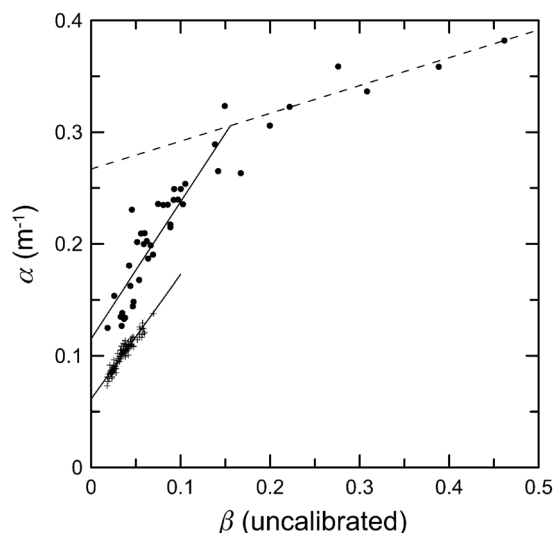


Fig. 7 Lidar attenuation coefficient, α , as a function of the uncalibrated volume backscatter function, β , near the surface for offshore (+) and nearshore (•) waters. Lines are regressions to the corresponding data outside (solid) and inside (dashed) the Columbia River plume. (Reproduced from Ref. 46).

specific absorption coefficient is defined as the absorption coefficient per unit of dissolved organic material. Using a value of $0.33 \text{ m}^{-1} (\text{mgCL}^{-1})^{-1}$ for the specific absorption coefficient at 450 nm (Ref. 92) and converting to 532 nm (Ref. 91), we get a specific absorption coefficient at the lidar wavelength of $0.10 \text{ m}^{-1} (\text{mgCL}^{-1})^{-1}$. Removing the clear-water absorption from the estimated Columbia River plume absorption and dividing by this specific absorption provides an estimate of $(0.27 - 0.05)/0.1 = 2.2 \text{ mgCL}^{-1}$. Recent measurements in the river have reported values of $2.0 \pm 0.3 \text{ mgCL}^{-1}$,⁹³ suggesting this might be a viable technique. The estimated uncertainty in the specific absorption coefficient is $\pm 50\%$ (Ref. 92), however, and more measurements of this quantity are needed.

There are two scattering parameters that are typically of interest—the scattering coefficient, b , and the backscattering coefficient b_b . With measured values for c and a , as above, the scattering coefficient can be obtained from $b = c - a$. The backscatter coefficient, of interest to remote sensing, is more difficult. However, the particulate volume scattering function normalized by b_b seems to have a fairly consistent shape for scattering angles between 90 and 170 deg.⁹⁴ This shape, based on three million measurements at 10 locations, was approximated by a fourth-order polynomial in Ref. 94, which can be extrapolated to a scattering angle of 180 deg. The result is that the particulate contribution b_{bp} can be estimated from the lidar measurement of $\beta(\pi)$ using the relationship

$$b_{bp} = 6.43[\beta(\pi) - 2.53 \times 10^{-4}], \quad (14)$$

where the constant within the square brackets is $\beta(\pi)$ for pure sea water at 532 nm. The total b_b is this value plus the pure water value of $1.11 \times 10^{-3} \text{ m}^{-1}$.

4.4 Upper Ocean Dynamics

The dynamics of the upper ocean are rather complex.⁹⁵ There is an ever-shifting balance between stratification and vertical

mixing. Stratification is enhanced by solar heating of the surface and by fresh-water influx from terrestrial runoff and melting ice. Mixing is enhanced by winds, wind-induced currents, tidal currents, and turbulence. The result is often an upper mixed layer with a density gradient, or pycnocline, at the bottom. The frequent association of plankton layers with the pycnocline⁷⁸ implies that the pycnocline depth can often be mapped by lidar.⁷⁷ Although most of these effects are local, internal waves caused by the interaction of tidal currents and bottom topography can propagate long distances on the pycnocline and produce mixing far from the source.^{96,97}

When plankton layers are present at the pycnocline, internal waves propagating on the pycnocline can be detected by lidar, and internal-wave observations have been reported by ship-based^{74,98} and airborne lidars.^{50,77,99} Large, nonlinear internal waves are easy to distinguish in lidar data, as in the example (Fig. 8) from airborne lidar in West Sound, Orcas Island, Washington.⁵⁰ The characteristics of these waves measured by the lidar can be used to infer characteristics of the mixed layer. To do this, the assumption is made that the density structure in the ocean can be approximated by two layers of different density with a scattering layer at the boundary. The thickness of the upper layer is obtained directly from the lidar, and the thickness of the lower layer is obtained from the total water depth provided by navigational charts. The amplitude of the wave is also directly measured by the lidar. More information requires a second pass of the lidar, so the propagation speed of the wave can be inferred. For a weakly nonlinear wave, the Korteweg–de Vries equation can be used to obtain the density difference between the upper and lower layers.⁵⁰ Combining this information, the total energy density within an internal-wave packet can be estimated.⁵⁰ In addition to the obvious nonlinear internal wave packets, the ocean has a random background field of weak internal waves that depend on wavenumber, κ , as $\kappa^{-5/3}$,¹⁰⁰ and this has also been observed by lidar.⁷⁷

The power spectrum of lidar backscatter also provides some insight into turbulent processes. For homogeneous, isotropic turbulence, the distribution of a passive tracer

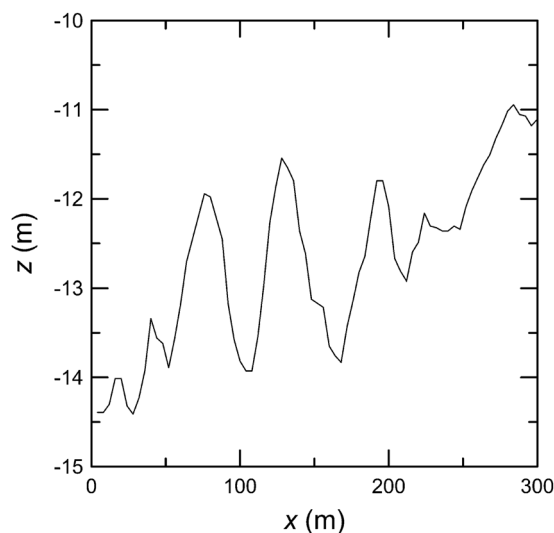


Fig. 8 Scattering layer depth, z , along 300 m of flight track, x . Internal wave has wavelength of 50 m and amplitude of 2 m.⁵⁰

would be expected to have a $\kappa^{-5/3}$ power spectrum. With few exceptions, phytoplankton drift with the local current and can be treated as a passive tracer, independent of their size and shape. Thus, lidar signal fluctuations would be expected to have a $\kappa^{-5/3}$ power spectrum when the distribution of phytoplankton is affected by turbulence. Lidar measurements of backscatter at constant depth in the NE Pacific Ocean, however, produced a spectral slope that was $\sim 10\%$ lower at -1.5 .¹⁰¹ The reason for the difference seems to be that this part of the ocean is not homogeneous, but stratified. Under these conditions, one would expect to find the $-5/3$ slope along a line of constant density, not constant depth,^{102,103} and this was observed in the lidar fluctuations along the center of a plankton layer.⁵⁰

4.5 Bubbles

Bubbles near the surface of the ocean, produced by breaking waves, affect a number of important processes. They facilitate the exchange of gases between the atmosphere and ocean^{104–106} and the production of cloud-condensing aerosols in the atmosphere.^{107,108} They produce sound in the ocean¹⁰⁹ and affect its propagation.^{110,111} Bubbles also scatter light, and the resulting change in ocean color can affect estimates of chlorophyll concentration based on the color of scattered light.^{112–114} While most of the bubbles are in the top 1 to 2 m of the ocean, breaking waves can produce plumes extending down to 20 m.¹¹⁵

The lidar return from bubbles has been theoretically estimated using Monte-Carlo simulation^{116,117} and geometric optics.¹¹⁸ The copolarized lidar return has been shown to be proportional to the total volume of air within the illuminated region, independent of the bubble size distribution as long as the bubbles are spherical and the density is low enough that multiple scattering can be neglected. A linear dependence of lidar signal on bubble number concentration has been verified in the laboratory.¹¹⁹ This suggests that a copolarized lidar receiver can provide profiles of bubble void fraction important to studies of air/sea gas exchange processes.

The utility of lidar for ship-wake measurements has been demonstrated in the laboratory,¹²⁰ and wakes have been

detected in the open ocean. Figure 9 is an example of the lidar return from the surface along a flight track that crossed the wakes of two boats, observed during a fisheries survey in Chesapeake Bay.⁶⁸ A photo of the surface shows the lidar track crossing two wakes. The stronger one (closer to the passage of the boat) shows the three lobes characteristic of the propeller wake and two hull wakes. In this case, the signal is partially depolarized by some combination of scattering from large, nonspherical bubbles and multiple scattering from the dense bubble cloud. In the weaker wake (farther behind the boat), the depolarization is too small to be detected. By this time, the larger bubbles have risen to the surface and the bubble density is lower.

5 Future Directions

5.1 Ocean Lidar Ratio

To date, techniques to simultaneously retrieve attenuation and scattering from lidar profiles have been limited to cases where these properties of the water column are slowly varying with depth. Figure 7 suggests that the particulate component of the lidar ratio for the ocean might be constant for a number of broad classes of water types, even though the actual value is not. The figure shows that the slopes are similar for both near-shore and offshore water outside of the Columbia River plume, whereas there is a different slope within the plume. If the intercept of the line (the absorption) is subtracted from the data, this produces one value of the lidar ratio within the plume and another outside of it. More studies of the lidar ratio for different water types can be expected in the future, both to improve lidar retrievals and to characterize different water types.

5.2 Temperature

Two different techniques have been investigated for temperature profiling in the ocean using inelastic scattering. Raman scattering excites a vibrational mode of the water molecule, which produces a frequency shift toward longer wavelengths over a broad band between 3000 and 3700 cm^{-1} . Brillouin scattering is from acoustic pressure fluctuations in the water and is Doppler shifted both up and down in frequency in a

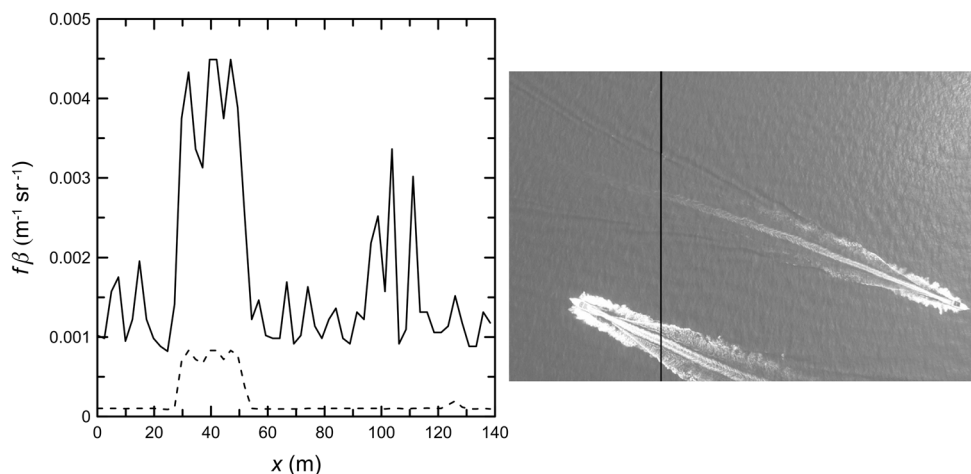


Fig. 9 Plot of fraction of lidar volume scattering coefficient, $f\beta$, for copolarized (solid line) and cross-polarized (dashed line) returns from the surface as functions of position along the flight track, x , over two boat wakes. The track in the plot follows the black line in the photo of the wakes from bottom to top.

narrow frequency band at 7.5 GHz (0.25 cm^{-1}). The scattering strength for these two processes, however, is $\sim 2 \times 10^{-4} \text{ m}^{-1} \text{ sr}^{-1}$ for both.¹²¹ Neither of these are new concepts, but the component technologies have not been suitable for widespread open-ocean application.

The Raman scattering approach uses the fact that water comprises clusters of molecules that are weakly bound (polymer form) and independent molecules (monomer form) whose relative concentrations are in thermodynamic equilibrium. As temperature increases, order decreases and the balance shifts toward a higher concentration of monomers. The Raman shift of the two forms are different—peaks at 3535 and 3622 cm^{-1} are from monomeric water and increase with increasing temperature, while peaks at 3247 and 3435 cm^{-1} are from polymeric water and decrease with increasing temperature.¹²² Thus, the ratio of the Raman return at two wavelengths can be used to infer temperature. For 532-nm illumination, one of the Raman-shifted wavelengths would be between the monomer peaks at 655 and 659 nm, and the other would be between the polymer peaks at 643 and 651 nm. Another difference between Raman scattering from monomer and polymer waters is that the former is not depolarized for polarized illumination, while the latter is. This implies that depolarization of the Raman signal can also be used to infer temperature.

Because the Raman-shifted light is strongly absorbed when 532-nm illumination is used, measurements have used shorter-wavelength lasers^{123–126} unless only near-surface values are required.^{127,128} Using this technique, temperature profiles have been measured to 30 m using a 450-nm laser on a ship.¹²³ However, the technique has not found wide application largely because of interference with background light over the broad Raman band, distortion of the spectrum by differential absorption over that same band, and practical problems associated with high-energy blue sources.

The frequency of the Brillouin return provides a measure of the speed of sound in the water, V , which depends on temperature, salinity, and pressure as¹²⁹

$$\begin{aligned} V &= 1449.22 + \Delta V_T + \Delta V_S + \Delta V_P + \Delta V_{TSP} \\ \Delta V_T &= 4.6233T - 5.4585 \times 10^{-2}T^2 + 2.822 \\ &\quad \times 10^{-4}T^3 - 5.07 \times 10^{-7}T^4 \\ \Delta V_S &= 1.391(S - 35) - 0.078(S - 35)^2 \\ \Delta V_P &= 0.160518P + 1.0279P^2 + 3.451 \\ &\quad \times 10^{-9}P^3 - 3.503 \times 10^{-12}P^4, \end{aligned} \quad (15)$$

where T is temperature ($^{\circ}\text{C}$), S is salinity (PSU), and P is pressure (kg cm^{-2}). Over the range of values typical of the upper 100 m of the ocean ($0 \text{ deg} < T < 30 \text{ deg}$, $33\text{‰} < S < 37\text{‰}$, $1 \text{ kg cm}^{-2} < P < 100 \text{ kg cm}^{-2}$), ΔV_T changes by 100 m s^{-1} , ΔV_S changes by 5.5 m s^{-1} , and ΔV_P changes by 16 m s^{-1} . A complicated combined term ΔV_{TSP} changes by $< 1 \text{ m s}^{-1}$, and is not reproduced here. P can be estimated from depth, so temperature can be estimated from sound speed within a few percent by assuming an average salinity and neglecting ΔV_{TSP} . The lidar Doppler shift for 532-nm laser light and a sound speed of 1500 m s^{-1} is 7.5 GHz, which is typically measured with an interferometer. An accuracy of 1°C implies a frequency measurement

with 20 MHz accuracy, requiring very precise optical interferometers.

Most of the work on ocean temperature sensing by Brillouin lidar has been theoretical analyses^{130–132} or laboratory demonstrations,^{133–135} as described in another paper in this issue.¹³⁶ It has not found widespread application because the required laser stability and receiver frequency accuracy have been difficult to obtain outside of the laboratory. These are both areas of active research,^{136–139} and the application of lidar profiling of temperature in the open ocean can be expected in the future.¹³⁶

5.3 High-Spectral-Resolution Lidar

The concept of a high-spectral-resolution lidar (HSRL) originated as a way to separate aerosol from molecular scattering in the atmosphere,^{140–142} based on the premise that the Doppler shift from aerosols is small compared with that from air molecules. This same concept can be applied to sea water in order to simultaneously measure attenuation and backscattering using a two-channel receiver.¹⁴³ The volume backscatter coefficient of pure seawater, β_{sw} , can be calculated precisely, since the density of water changes very little in the upper 50 to 100 m. Over 98% of this scattered light is in the two symmetric Brillouin peaks Doppler shifted up or down by 7.5 GHz (7 pm for an initial wavelength of 532 nm).¹⁴⁴ The Doppler shift from particulate scattering is very small, so one of the two receiver channels is equipped with a spectral filter that only passes the Brillouin peaks. The signal from this channel is inverted using Eq. (1), with $\beta = \beta_{\text{sw}}$, to obtain $\alpha(z)$. The other receiver channel responds to both seawater and particulate scattering. The signal from this channel is inverted using $\alpha(z)$, obtained from the Brillouin channel, in Eq. (1) to obtain $\beta(z)$, which, for this channel, is the sum of seawater and particulate components. An optical filter to pass the Brillouin return is much simpler than an interferometer to precisely measure its frequency, so the application of HSRL to measure attenuation and scattering in the ocean can be expected earlier than temperature profiling using the Brillouin technique.

5.4 Space-Based Lidar

The cloud-aerosol lidar with orthogonal polarization on the CALIPSO satellite was launched to study clouds and aerosols in the atmosphere,¹⁴⁵ but has co- and cross-polarized receivers for the 532-nm laser light. This similarity has motivated several studies into possible ocean subsurface returns.^{146,147} However, the range-resolution of this lidar was designed with atmospheric studies in mind. Near the surface, the sample frequency is 5 MHz, which corresponds to a range resolution of 22.5 m in water. Prior to sampling, the signal has been low-pass filtered with a 2-MHz filter, so the strong surface return extends over three samples. In addition, the photomultipliers have a slowly decaying tail from signal-induced fluorescence within the tubes.¹⁴⁸ The result of these two effects is an impulse-response function given by¹⁴⁹

$$\begin{aligned} g_T &= \exp\left[-\left(\frac{z}{15}\right)^2\right] + 0.015 \exp\left(-\frac{z}{118}\right) \quad \text{and} \\ g_X &= \exp\left[-\left(\frac{z}{15}\right)^2\right] + 0.014 \exp\left(-\frac{z}{110}\right) \end{aligned} \quad (16)$$

for the unpolarized and cross-polarized receiver channels, respectively. These two effects mask the subsurface return under most conditions.

Despite these limitations, there is evidence of subsurface return in the cross-polarized lidar channel at the two sample depths of 28 and 50 m,¹⁴⁹ and it seems feasible to build a space-based lidar with depth resolution of a meter or so, better matched to oceanographic requirements.^{150,151} Coupled with ocean color measurements, this would be a powerful tool for global observations of the upper ocean.

6 Conclusions

This paper has described the characteristics of the critical lidar components that need to be considered in the design. For many applications, Q-switched, frequency-doubled Nd:YAG will be the clear choice for a laser, in no small part because of its reliable operation in the field. For open-ocean applications, a blue laser would provide better depth penetration, but the technology is more complex. The two receiver characteristics that must be carefully considered are field of view and dynamic range. For many applications, a wider field of view will be desired to minimize the attenuation of the signal with depth, even though this will result in increased levels of background light. There are several approaches to maximizing dynamic range, all of which have advantages and disadvantages. The eventual solution will be a high-speed digitizer with sufficient dynamic range, and this is probably not too far off.

This paper has described the basic equations describing the performance of profiling lidars. Because of its simplicity, the quasi-single-scattering approximation is the best choice for many applications. The extension of this theoretical approach to include polarization was also described. This extension led to the conclusion that linear and circular polarizations are equivalent in the information content, but circular polarization might be better from a signal-to-noise consideration.

This paper has described applications of lidar for profiling several properties of the upper ocean. These properties include the vertical distribution of fish, plankton, bubbles, and the optical properties of scattering, absorption, and attenuation that are affected by suspended sediments and dissolved substances. Lidar has also been shown to be useful in understanding the dynamical properties of the upper ocean. Scattering particles move with the water and act as tracers for mixing processes like internal waves and turbulence. They are also often associated with the pycnocline, which identifies the depth of the oceanic mixed layer. The conclusion was that a great deal of information about the upper ocean can be obtained from lidar systems. This information has relevance to physical, biological, and chemical oceanography.

This paper has described several areas where progress in lidar profiling can be expected in the future. Quantitative retrievals of atmospheric lidars have been improved by applications of HSRL techniques and by thorough investigations of the lidar ratio in different atmospheric conditions. These same techniques will be applied to oceanographic lidars, and similar progress is expected. Technological advances, especially in the area of stable lasers and filters, are likely to lead to practical application of lidar temperature profiling. Farther into the future, global coverage from an oceanographic lidar operating from a satellite is likely.

References

1. C. R. McClain, "A decade of satellite ocean color observations," *Ann. Rev. Mar. Sci.* **1**(1), 19–42 (2009).
2. D. A. Siegel et al., "Regional to global assessments of phytoplankton dynamics from the SeaWiFS mission," *Remote Sens. Environ.* **135**, 77–91 (2013).
3. M. J. Behrenfeld and P. G. Falkowski, "Photosynthetic rates derived from satellite-based chlorophyll concentration," *Limnol. Oceanogr.* **42**(1), 1–20 (1997).
4. T. Westberry et al., "Carbon-based primary productivity modeling with vertically resolved photoacclimation," *Global Biogeochem. Cycles* **22**(2), GB2024 (2008).
5. J. Busck, "Underwater 3-D optical imaging with a gated viewing laser radar," *Opt. Eng.* **44**(11), 116001 (2005).
6. B. Cochenour, L. Mullen, and J. Muth, "Modulated pulse laser with pseudorandom coding capabilities for underwater ranging, detection, and imaging," *Appl. Opt.* **50**(33), 6168–6178 (2011).
7. J. H. Churnside and J. J. Wilson, "Airborne lidar imaging of salmon," *Appl. Opt.* **43**(6), 1416–1424 (2004).
8. G. C. Guenther, M. W. Brooks, and P. E. LaRocque, "New capabilities of the 'SHOALS' airborne lidar bathymeter," *Remote Sens. Environ.* **73**(2), 247–255 (2000).
9. C. W. Finkl, L. Benedet, and J. L. Andrews, "Submarine geomorphology of the continental shelf off southeast Florida based on interpretation of airborne laser bathymetry," *J. Coastal Res.* **21**(6), 1178–1190 (2005).
10. J. A. Yoder et al., "Spatial variability in near-surface chlorophyll a fluorescence measured by the airborne oceanographic lidar (AOL)," *Deep Sea Res. Part 2 Top. Stud. Oceanogr.* **40**(1–2), 37–53 (1993).
11. I. Leifer et al., "State of the art satellite and airborne marine oil spill remote sensing: application to the BP deepwater horizon oil spill," *Remote Sens. Environ.* **124**, 185–209 (2012).
12. A. Chekalyuk and M. Hafez, "Advanced laser fluorometry of natural aquatic environments," *Limnol. Oceanogr. Methods* **6**(11), 591–609 (2008).
13. Y. Hu et al., "Sea surface wind speed estimation from space-based lidar measurements," *Atmos. Chem. Phys.* **8**(13), 3593–3601 (2008).
14. J. A. Shaw and J. H. Churnside, "Scanning-laser glint measurements of sea-surface slope statistics," *Appl. Opt.* **36**(18), 4202–4213 (1997).
15. C. Flamant et al., "Analysis of surface wind and roughness length evolution with fetch using a combination of airborne lidar and radar measurements," *J. Geophys. Res.* **108**(C3), 8058 (2003).
16. A. Morel, "Light and marine photosynthesis: a spectral model with geochemical and climatological implications," *Prog. Oceanogr.* **26**(3), 263–306 (1991).
17. C. D. Mobley, *Light and Water: Radiative Transfer in Natural Waters*, Academic Press, San Diego (1994).
18. A. Bricaud, A. Morel, and L. Preiur, "Absorption by dissolved organic matter of the sea (yellow substance) in the UV and visible domains," *Limnol. Oceanogr.* **26**(1), 43–53 (1981).
19. C. S. Roesler, M. J. Perry, and K. L. Carder, "Modeling in situ phytoplankton absorption from total absorption spectra in productive inland marine waters," *Limnol. Oceanogr.* **34**(8), 1510–1523 (1989).
20. J. H. Churnside, J. J. Wilson, and V. V. Tatarskii, "Lidar profiles of fish schools," *Appl. Opt.* **36**(24), 6011–6020 (1997).
21. M. P. Bristow, "Lidar-signal compression by photomultiplier gain modulation: influence of detector nonlinearity," *Appl. Opt.* **37**(27), 6468–6479 (1998).
22. M. H. Sweet, "A logarithmic photo-multiplier tube photo-meter," *J. Opt. Soc. Am.* **37**(6), 432–432 (1947).
23. J. H. Churnside and J. J. Wilson, "Airborne lidar for fisheries applications," *Opt. Eng.* **40**(3), 406–414 (2001).
24. P. Carrera et al., "Comparison of airborne lidar with echosounders: a case study in the coastal Atlantic waters of southern Europe," *ICES J. Mar. Sci.* **63**(9), 1736–1750 (2006).
25. G. P. Kokhanenko, I. E. Penner, and V. S. Shamanaev, "Expanding the dynamic range of a lidar receiver by the method of dynode-signal collection," *Appl. Opt.* **41**(24), 5073–5077 (2002).
26. M. G. Löfdahl, V. M. J. Henriques, and D. Kiselman, "A tilted interference filter in a converging beam," *Astron. Astrophys.* **533**, A82 (2011).
27. W. W. Gregg and K. L. Carder, "A simple spectral solar irradiance model for cloudless maritime atmospheres," *Limnol. Oceanogr.* **35**(8), 1657–1675 (1990).
28. J. H. Lee et al., "Oceanographic lidar profiles compared with estimates from in situ optical measurements," *Appl. Opt.* **52**(4), 786–794 (2013).
29. J. L. Bufton, F. E. Hoge, and R. N. Swift, "Airborne measurements of laser backscatter from the ocean surface," *Appl. Opt.* **22**(17), 2603–2618 (1983).
30. G. W. Kattawar and G. N. Plass, "Time of flight lidar measurements as an ocean probe," *Appl. Opt.* **11**(3), 662–666 (1972).
31. H. R. Gordon, "Interpretation of airborne oceanic lidar: effects of multiple scattering," *Appl. Opt.* **21**(16), 2996–3001 (1982).
32. M. M. Krekova et al., "Numerical evaluation of the possibilities of remote laser sensing of fish schools," *Appl. Opt.* **33**(24), 5715–5720 (1994).

33. G. M. Krekov, M. M. Krekova, and V. S. Shamanaev, "Laser sensing of a subsurface oceanic layer. I. Effect of the atmosphere and wind-driven sea waves," *Appl. Opt.* **37**(9), 1589–1595 (1998).
34. G. M. Krekov, M. M. Krekova, and V. S. Shamanaev, "Laser sensing of a subsurface oceanic layer. II. Polarization characteristics of signals," *Appl. Opt.* **37**(9), 1596–1601 (1998).
35. R. E. Walker, *Marine Light Field Statistics*, John Wiley and Sons, New York (1994).
36. K. Stamnes et al., "Numerically stable algorithm for discrete-ordinate-method radiative transfer in multiple scattering and emitting layered media," *Appl. Opt.* **27**(12), 2502–2509 (1988).
37. K. I. Gjerstad et al., "Monte Carlo and discrete-ordinate simulations of irradiances in the coupled atmosphere-ocean system," *Appl. Opt.* **42**(15), 2609–2622 (2003).
38. K. Mitra and J. H. Churnside, "Transient radiative transfer equation applied to oceanographic lidar," *Appl. Opt.* **38**(6), 889–895 (1999).
39. M. Chami, R. Santer, and E. Dilligeard, "Radiative transfer model for the computation of radiance and polarization in an ocean-atmosphere system: polarization properties of suspended matter for remote sensing," *Appl. Opt.* **40**(15), 2398–2416 (2001).
40. P.-W. Zhai et al., "A vector radiative transfer model for coupled atmosphere and ocean systems based on successive order of scattering method," *Opt. Express* **17**(4), 2057–2079 (2009).
41. L. S. Dolin and V. A. Saveliev, "Backscattering signal in pulsed irradiation of a turbid medium with a narrow, directional light beam," *Izvestiya Akademii Nauk SSSR seriya Fizika Atmosfery i Okeana* **7**(7), 505–510 (1971).
42. I. L. Katsev et al., "Efficient technique to determine backscattered light power for various atmospheric and oceanic sounding and imaging systems," *J. Opt. Soc. Am. A* **14**(6), 1338–1346 (1997).
43. H. R. Gordon, "Simple calculation of the diffuse reflectance of the ocean," *Appl. Opt.* **12**(12), 2803–2804 (1973).
44. H. R. Gordon, "Can the Lambert-Beer law be applied to the diffuse attenuation coefficient of ocean water?," *Limnol. Oceanogr.* **34**(8), 1389–1409 (1989).
45. Z.-P. Lee et al., "Diffuse attenuation coefficient of downwelling irradiance: an evaluation of remote sensing methods," *J. Geophys. Res.* **110**(C2), C02017 (2005).
46. J. H. Churnside, "Polarization effects on oceanographic lidar," *Opt. Express* **16**(2), 1196–1207 (2008).
47. H. C. van de Hulst, *Light Scattering by Small Particles*, Dover, New York (1981).
48. M. I. Mishchenko and J. W. Hovenier, "Depolarization of light backscattered by randomly oriented nonspherical particles," *Opt. Lett.* **20**(12), 1356–1358 (1995).
49. G. G. Gimmetstad, "Reexamination of depolarization in lidar measurements," *Appl. Opt.* **47**(21), 3795–3802 (2008).
50. J. H. Churnside et al., "Airborne lidar detection and characterization of internal waves in a shallow fjord," *J. Appl. Remote Sens.* **6**(1), 63611–63615 (2012).
51. D. Sliney and M. Wolbarsht, *Safety with Lasers and other Optical Sources*, Plenum Press, New York (1980).
52. K. M. Hock, "Probability theory of laser safety at sea," *Opt. Eng.* **35**(4), 1098–1104 (1996).
53. H. M. Zorn, J. H. Churnside, and C. W. Oliver, "Laser safety thresholds for cetaceans and pinnipeds," *Mar. Mammal Sci.* **16**(1), 186–200 (2000).
54. American National Standards Institute, *American National Standard for Safe Use of Lasers*, p. 249, Laser Institute of America, Orlando, Florida (2007).
55. American National Standards Institute, *American National Standard for Safe use of Lasers Outdoors*, p. 116, Laser Institute of America, Orlando, Florida (2005).
56. D. L. Murphree, C. D. Taylor, and R. W. McClendon, "Mathematical modeling for the detection of fish by an airborne laser," *AIAA J.* **12**(12), 1686–1692 (1974).
57. J. L. Squire and H. Krumboltz, "Profiling pelagic fish schools using airborne optical lasers and other remote sensing techniques," *Mar. Tech. Soc. J.* **15**(4), 29–31 (1981).
58. K. Fredriksson et al., "Marine laser probing: results from a field test," in *Meddelande fran Havsfiskelaboratoriet, Lysekil*, 21 p, Chalmers Institute of Technology, Goteborg (1979).
59. N. C. H. Lo, J. R. Hunter, and J. H. Churnside, "Modeling statistical performance of an airborne lidar survey system for anchovy," *Fish. Bull.* **98**(2), 264–282 (2000).
60. J. H. Churnside, K. Sawada, and T. Okumura, "A comparison of lidar and echo sounder performance in fisheries," *J. Mar. Acoust. Soc. Jpn.* **28**(3), 175–187 (2001).
61. J. H. Churnside et al., "Comparisons of lidar, acoustic and trawl data on two scales in the Northeast Pacific Ocean," *CalCOFI Rep.* **50**, 118–122 (2009).
62. J. H. Churnside, D. A. Demer, and B. Mahmoudi, "A comparison of lidar and echosounder measurements of fish schools in the Gulf of Mexico," *ICES J. Mar. Sci.* **60**(1), 147–154 (2003).
63. E. D. Brown et al., "Remote sensing of capelin and other biological features in the North Pacific using lidar and video technology," *ICES J. Mar. Sci.* **59**(7), 1120–1130 (2002).
64. J. H. Churnside, E. Tenningen, and J. J. Wilson, "Comparison of data-processing algorithms for the lidar detection of mackerel in the Norwegian Sea," *ICES J. Mar. Sci.* **66**(6), 1023–1028 (2009).
65. K. Fredriksson et al., "Underwater laser-radar experiments for bathymetry and fish-school detection," in *Göteborg Institute of Physics Reports*, 28 p, Chalmers Institute of Technology, Göteborg, Sweden (1978).
66. J. H. Churnside and P. A. Mcgillivray, "Optical properties of several Pacific fishes," *Appl. Opt.* **30**(21), 2925–2927 (1991).
67. E. Tenningen et al., "Lidar target-strength measurements on Northeast Atlantic mackerel (*Scomber scombrus*)," *ICES J. Mar. Sci.* **63**(4), 677–682 (2006).
68. J. H. Churnside, A. F. Sharov, and R. A. Richter, "Aerial surveys of fish in estuaries: a case study in Chesapeake Bay," *ICES J. Mar. Sci.* **68**(1), 239–244 (2011).
69. J. H. Churnside and R. E. Thorne, "Comparison of airborne lidar measurements with 420 kHz echo-sounder measurements of zooplankton," *Appl. Opt.* **44**(26), 5504–5511 (2005).
70. D. C. Reese et al., "Epipelagic fish distributions in relation to thermal fronts in a coastal upwelling system using high-resolution remote-sensing techniques," *ICES J. Mar. Sci.* **68**(9), 1865–1874 (2011).
71. R. W. Gauldie, S. K. Sharma, and C. E. Helsley, "Lidar applications to fisheries monitoring problems," *Can. J. Fish. Aquat. Sci.* **56**(6), 1459–1468 (1996).
72. J. H. Churnside et al., "Airborne remote sensing of a biological hot spot in the Southeastern Bering Sea," *Remote Sens.* **3**(3), 621–637 (2011).
73. A. De Robertis and N. O. Handegard, "Fish avoidance of research vessels and the efficacy of noise-reduced vessels: a review," *ICES J. Mar. Sci.* **70**(1), 34–45 (2013).
74. O. A. Bukin et al., "Measurement of the lightscattering layers structure and detection of the dynamic processes in the upper ocean layer by shipborne lidar," *Int. J. Remote Sens.* **19**(4), 707–715 (1998).
75. F. E. Hoge et al., "Airborne lidar detection of subsurface oceanic scattering layers," *Appl. Opt.* **27**(19), 3969–3977 (1988).
76. A. P. Vasilkov et al., "Airborne polarized lidar detection of scattering layers in the ocean," *Appl. Opt.* **40**(24), 4353–4364 (2001).
77. J. H. Churnside and P. L. Donaghay, "Thin scattering layers observed by airborne lidar," *ICES J. Mar. Sci.* **66**(4), 778–789 (2009).
78. M. M. Dekshenieks et al., "Temporal and spatial occurrence of thin phytoplankton layers in relation to physical processes," *Mar. Ecol. Prog. Ser.* **223**, 61–71 (2001).
79. W. M. Durham and R. Stocker, "Thin phytoplankton layers: characteristics, mechanisms, and consequences," *Ann. Rev. Mar. Sci.* **4**(1), 177–207 (2012).
80. A. K. Hanson and P. L. Donaghay, "Micro- to fine-scale chemical gradients and layers in stratified coastal waters," *Oceanography* **11**(1), 10–17 (1998).
81. J. M. Sullivan, P. L. Donaghay, and J. E. B. Rines, "Coastal thin layer dynamics: consequences to biology and optics," *Cont. Shelf Res.* **30**(1), 50–65 (2010).
82. A. Romanou et al., "Natural air-sea flux of CO₂ in simulations of the NASA-GISS climate model: sensitivity to the physical ocean model formulation," *Ocean Model.* **66**, 26–44 (2013).
83. M. A. Brzezinski, "The Si:C:N ratio of marine diatoms: interspecific variability and the effect of some environmental variables," *J. Phycol.* **21**(3), 347–357 (1985).
84. J. R. V. Zaneveld and W. S. Pegau, "A model for the reflectance of thin layers, fronts, and internal waves and its inversion," *Oceanography* **11**(1), 44–47 (1998).
85. J. M. Sullivan et al., "Use of optical scattering to discriminate particle types in coastal waters," *Appl. Opt.* **44**(9), 1667–1680 (2005).
86. M. A. Montes-Hugo et al., "Ocean color patterns help to predict depth of optical layers in stratified coastal waters," *J. Appl. Remote Sens.* **5**(1), 05354 (2011).
87. M. A. Montes-Hugo et al., "Spatial coherence between remotely sensed ocean color data and vertical distribution of lidar backscattering in coastal stratified waters," *Remote Sens. Environ.* **114**(11), 2584–2593 (2010).
88. A. H. Omar et al., "The CALIPSO automated aerosol classification and lidar ratio selection algorithm," *J. Atmos. Ocean. Technol.* **26**(10), 1994–2014 (2009).
89. J. H. Churnside, V. V. Tatarskii, and J. J. Wilson, "Oceanographic lidar attenuation coefficients and signal fluctuations measured from a ship in the Southern California Bight," *Appl. Opt.* **37**(15), 3105–3112 (1998).
90. M. A. Montes et al., "Relationships between water attenuation coefficients derived from active and passive remote sensing: a case study from two coastal environments," *Appl. Opt.* **50**(18), 2990–2999 (2011).
91. V. S. Shamanaev et al., "Hydrooptical laser sensing under controllable conditions," *Russ. Phys. J.* **48**(12), 1251–1256 (2005).
92. M. S. Twardowski and P. L. Donaghay, "Photobleaching of aquatic dissolved materials: absorption removal, spectral alteration, and their interrelationship," *J. Geophys. Res.* **107**(C8), 6-1–6-12 (2002).

93. R. G. M. Spencer, K. D. Butler, and G. R. Aiken, "Dissolved organic carbon and chromophoric dissolved organic matter properties of rivers in the USA," *J. Geophys. Res.* **117**(G3), G03001 (2012).
94. J. M. Sullivan and M. S. Twardowski, "Angular shape of the oceanic particulate volume scattering function in the backward direction," *Appl. Opt.* **48**(35), 6811–6819 (2009).
95. J. F. Price, E. A. Terray, and R. A. Weller, "Upper ocean dynamics," *Rev. Geophys.* **25**(2), 193–203 (1987).
96. C. Garrett, "Internal tides and ocean mixing," *Science* **301**(5641), 1858–1859 (2003).
97. M. H. Alford, "Redistribution of energy available for ocean mixing by long-range propagation of internal waves," *Nature* **423**(6936), 159–162 (2003).
98. L. S. Dolin, I. S. Dolina, and V. A. Savel'ev, "A lidar method for determining internal wave characteristics," *Izvestiya Atmos. Ocean. Phys.* **48**(4), 444–453 (2012).
99. J. H. Churnside and L. A. Ostrovsky, "Lidar observation of a strongly nonlinear internal wave train in the Gulf of Alaska," *Int. J. Remote Sens.* **26**(1), 167–177 (2005).
100. C. Garrett and W. Munk, "Internal waves in the ocean," *Ann. Rev. Fluid Mech.* **11**(1), 339–369 (1979).
101. J. H. Churnside and J. J. Wilson, "Power spectrum and fractal dimension of laser backscattering from the ocean," *J. Opt. Soc. Am. A* **23**(11), 2829–2833 (2006).
102. J. J. Riley and E. Lindborg, "Stratified turbulence: a possible interpretation of some geophysical turbulence measurements," *J. Atmos. Sci.* **65**(7), 2416–2424 (2008).
103. E. Lindborg, "The energy cascade in a strongly stratified fluid," *J. Fluid Mech.* **550**, 207–242 (2006).
104. D. K. Woolf, "Bubbles and the air-sea transfer velocity of gases," *Atmosphere-Ocean* **31**(4), 517–540 (1993).
105. R. S. Bortkovskii et al., "Model estimates for the mean gas exchange between the ocean and the atmosphere under the conditions of the present-day climate and its changes expected in the 21st century," *Izvestiya Atmos. Ocean. Phys.* **43**(3), 378–383 (2007).
106. X. Zhang, "Contribution to the global air-sea CO₂ exchange budget from asymmetric bubble-mediated gas transfer," *Tellus B* **64**, 17260 (2012).
107. W. C. Keene et al., "Chemical and physical characteristics of nascent aerosols produced by bursting bubbles at a model air-sea interface," *J. Geophys. Res.* **112**(D21), D21202 (2007).
108. A. Sorooshian et al., "On the link between ocean biota emissions, aerosol, and maritime clouds: airborne, ground, and satellite measurements off the coast of California," *Global Biogeochem. Cycles* **23**(4), GB4007 (2009).
109. M. R. Loewen and W. K. Melville, "An experimental investigation of the collective oscillations of bubble plumes entrained by breaking waves," *J. Acoust. Soc. Am.* **95**(3), 1329–1343 (1994).
110. M. V. Hall, "A comprehensive model of wind-generated bubbles in the ocean and predictions of the effects on sound propagation at frequencies up to 40 kHz," *J. Acoust. Soc. Am.* **86**(3), 1103–1117 (1989).
111. P. A. Hwang and W. J. Teague, "Low-frequency resonant scattering of bubble clouds," *J. Atmos. Ocean. Technol.* **17**(6), 847–853 (2000).
112. X. Zhang, M. Lewis, and B. Johnson, "Influence of bubbles on scattering of light in the ocean," *Appl. Opt.* **37**(27), 6525–6536 (1998).
113. E. J. Terrill, W. K. Melville, and D. Stramski, "Bubble entrainment by breaking waves and their influence on optical scattering in the upper ocean," *J. Geophys. Res.* **106**(C8), 16815–16823 (2001).
114. X. Zhang et al., "The volume scattering function of natural bubble populations," *Limnol. Oceanogr.* **47**(7), 1273–1282 (2002).
115. M. V. Trevorow, "Measurements of near-surface bubble plumes in the open ocean with implications for high-frequency sonar performance," *J. Acoust. Soc. Am.* **114**(7), 2672–2684 (2003).
116. M. M. Krekova, G. M. Krekov, and V. S. Shamaev, "Influence of air bubbles in seawater on the formation of lidar returns," *J. Atmos. Ocean. Technol.* **21**(7), 819–824 (2004).
117. X. Min et al., "Monte Carlo simulation of backscattering signal from bubbles under water," *J. Opt. A Pure Appl. Opt.* **8**(3), 350 (2006).
118. J. H. Churnside, "Lidar signature from bubbles in the sea," *Opt. Express* **18**(8), 8294–8299 (2010).
119. W. Li et al., "Influence of characteristics of micro-bubble clouds on backscatter lidar signal," *Opt. Express* **17**(20), 17772–17783 (2009).
120. S. Liping et al., "Simple lidar detecting wake profiles," *J. Opt. A Pure Appl. Opt.* **9**(10), 842 (2007).
121. D. A. Leonard and H. E. Sweeney, "Remote sensing of ocean physical properties: a comparison of Raman and Brillouin techniques," *Proc. SPIE* **0925**, 407–414 (1988).
122. G. E. Walrafen, "Raman spectral studies of the effects of temperature on water structure," *J. Chem. Phys.* **47**(1), 114–126 (1967).
123. D. A. Leonard, B. Caputo, and F. E. Hoge, "Remote sensing of subsurface water temperature by Raman scattering," *Appl. Opt.* **18**(11), 1732–1745 (1979).
124. D. A. Leonard and B. Caputo, "Raman remote sensing of the ocean mixed-layer depth," *Opt. Eng.* **22**(3), 288–291 (1983).
125. D. A. Leonard and B. Caputo, "Raman LIDAR for the remote measurement of subsurface ocean parameters," *Proc. SPIE* **0489**, 277–280 (1984).
126. D. A. Leonard et al., "Experimental remote sensing of subsurface temperature in natural ocean water," *Geophys. Res. Lett.* **4**(7), 279–281 (1977).
127. S. M. Pershin et al., "Remote sensing of Arctic Fjords by Raman lidar: heat transfer screening by layer of glacier's relic water," *Phys. Wave Phenom.* **20**(3), 212–222 (2012).
128. A. F. Bunkin et al., "Remote sensing of seawater and drifting ice in Svalbard fjords by compact Raman lidar," *Appl. Opt.* **51**(22), 5477–5485 (2012).
129. W. D. Wilson, "Speed of sound in sea water as a function of temperature, pressure, and salinity," *J. Acoust. Soc. Am.* **32**(6), 641–644 (1960).
130. G. D. Hickman et al., "Aircraft laser sensing of sound velocity in water: Brillouin scattering," *Remote Sens. Environ.* **36**(3), 165–178 (1991).
131. B. D. Joelson and G. W. Kattawar, "Multiple scattering effects on the remote sensing of the speed of sound in the ocean by Brillouin scattering," *Appl. Opt.* **35**(15), 2693–2701 (1996).
132. E. S. Fry et al., "Accuracy limitations on Brillouin lidar measurements of temperature and sound speed in the ocean," *Appl. Opt.* **36**(27), 6887–6894 (1997).
133. J. G. Hirschberg et al., "Speed of sound and temperature in the ocean by Brillouin scattering," *Appl. Opt.* **23**(15), 2624–2628 (1984).
134. D. Liu et al., "Measurements of sound speed in the water by Brillouin scattering using pulsed Nd:YAG laser," *Opt. Commun.* **203**(3–6), 335–340 (2002).
135. K. Liang et al., "Research on simultaneous measurement of ocean temperature and salinity using Brillouin shift and linewidth," *Opt. Eng.* **51**(6), 066002 (2012).
136. A. Rudolf and T. Walther, "Laboratory demonstration of a Brillouin lidar to remotely measure temperature profiles of the ocean," *Opt. Eng.* **56**(7) (in press).
137. K. Schorstein et al., "Remote water temperature measurements based on Brillouin scattering with a frequency doubled pulsed Yb:doped fiber amplifier," *Sensors* **8**(9), 5820–5831 (2008).
138. E. S. Fry, "Remote sensing of sound speed in the ocean via Brillouin scattering," *Proc. SPIE* **8372**, 837207 (2012).
139. J. Shi et al., "A Brillouin lidar system using F-P etalon and ICCD for remote sensing of the ocean," *Appl. Phys. B* **90**(3–4), 569–571 (2008).
140. S. T. Shipley et al., "High spectral resolution lidar to measure optical scattering properties of atmospheric aerosols. 1: theory and instrumentation," *Appl. Opt.* **22**(23), 3716–3724 (1983).
141. P. Piironen and E. W. Eloranta, "Demonstration of a high-spectral-resolution lidar based on an iodine absorption filter," *Opt. Lett.* **19**(3), 234–236 (1994).
142. J. W. Hair et al., "Airborne high spectral resolution lidar for profiling aerosol optical properties," *Appl. Opt.* **47**(36), 6734–6752 (2008).
143. H. E. Sweeney, P. J. Titterton, and D. A. Leonard, *Method of Remotely Measuring Diffuse Attenuation Coefficient of Sea Water*, p. 15, GTE Government Systems Corporation, United States of America (1991).
144. C. L. O'Connor and J. P. Schlupf, "Brillouin scattering in water: the Landau-Placzek ratio," *J. Chem. Phys.* **47**(1), 31–38 (1967).
145. W. H. Hunt et al., "CALIPSO lidar description and performance assessment," *J. Atmos. Ocean. Technol.* **26**(7), 1214–1228 (2009).
146. W. Shi and M. Wang, "Three-dimensional observations from MODIS and CALIPSO for ocean responses to cyclone Nargis in the Gulf of Martaban," *Geophys. Res. Lett.* **35**(21), L21603 (2008).
147. J. S. Barton and M. F. Jasinski, "Sensitivity of depth-integrated satellite lidar to subaqueous scattering," *Remote Sens.* **3**(7), 1492–1515 (2011).
148. Y. Zhao, "Signal-induced fluorescence in photomultipliers in differential absorption lidar systems," *Appl. Opt.* **38**(21), 4639–4648 (1999).
149. J. H. Churnside, B. J. McCarty, and X. Lu, "Subsurface ocean signals from an orbiting polarization lidar," *Remote Sens.* **5**(7), 3457–3475 (2013).
150. H. R. Gordon, "Estimation of space-borne lidar return from natural waters: a passive approach," *Opt. Express* **17**(6), 4677–4684 (2009).
151. M. Stephens et al., "On-orbit models of the CALIOP lidar for enabling future mission design," *Proc. SPIE* **7807**, 78070F (2010).

James H. Churnside received his PhD from the Oregon Graduate Center studying the statistics of optical propagation through refractive turbulence in the clear atmosphere. He then became a member of the technical staff of The Aerospace Corporation in Los Angeles working on atmospheric propagation and laser speckle statistics. Since 1985, he has been a physicist with the NOAA Earth System Research Laboratory and its predecessors. He is currently working on the development of airborne oceanographic lidar and applications to fisheries, marine ecosystems, and upper ocean dynamics. He has published 93 papers in peer-reviewed journals and holds four patents.